Gradient-Based Predictive Pulse Pattern Control for Grid-Connected Converters with LCL Filters

Petros Karamanakos
Faculty of Inf. Technol. and Commun. Sciences
Tampere University
Tampere, Finland
p.karamanakos@ieee.org

Mirza Abdul Waris Begh
Faculty of Inf. Technol. and Commun. Sciences
Tampere University
Tampere, Finland
mirza.begh@tuni.fi

Shirin Rahmanpour
Faculty of Inf. Technol. and Commun. Sciences
Tampere University
Tampere, Finland
shirin.rahmanpour@tuni.fi

Tobias Geyer
Motion System Drives
ABB Switzerland Ltd
Turgi, Switzerland
t.geyer@ieee.org

***Abstract*—This paper presents a control algorithm for medium-voltage (MV) grid-connected converters with LCL filters. The controller is designed in the framework of model predictive control (MPC) to successfully address the multiple-input multiple-output characteristics of the system and provide active damping such that the apparent switching frequency of the converter can be equal to the filter resonance frequency. However, operation at such low switching frequencies—in the range of a few hundred hertz—requires filters with strong harmonic attenuation capabilities such that the low-order harmonics can be effectively mitigated. To avoid excessively bulky filters, while still meeting the relevant harmonic grid standards, optimized pulse patterns (OPPs) are employed and manipulated in a closed-loop fashion in real time. In doing so, the designed control algorithm ensures that low grid current harmonic distortions are produced, thus achieving excellent system performance. The effectiveness of the proposed control strategy is verified with an MV system consisting of a three-level neutral-point-clamped converter connected to the grid via an LCL filter.**

***Index Terms*—Medium-voltage (MV) converters, grid-connected power converters, model predictive control (MPC), optimal control, optimized pulse patterns (OPPs), multiple-input multiple-output (MIMO) control**

I. Introduction

Medium-voltage (MV) power converters connected to the grid via LCL filters[1] need to be operated such that requirements dictated by grid standards—such as limits on the total demand distortion (TDD) and the harmonics injected into the point of common coupling (PCC)—are fully respected. To do so, control algorithms need to successfully fulfill the demanding control objectives. However, as the systems in question exhibit multiple-input multiple-output (MIMO) characteristics, the controller design tends to become challenging [1]. This becomes even more complicated since MV systems need to be operated at switching frequencies of a few hundred hertz such that the power losses are kept low.

At such low switching frequencies, however, conventional control methods tend to be ineffective due to the limited decoupling of the control loops, thus deteriorating the system performance. Moreover, conventional modulation methods employed to generate the switching commands, such as carrier-based pulse width modulation (CB-PWM) or space vector modulation (SVM), perform poorly at such low switching frequencies [2], [3]. This is particularly the case when the ratio between switching and resonance frequency needs to be low to avoid oversizing of the line LCL filter. For this reason, conventional controllers—which typically consist of single-input single-output (SISO) loops arranged in a cascaded manner—are usually augmented with active damping loops to avoid excitation of the filter resonance [4], [5]. This, however, further complicates the controller design and compromises the dynamic performance of the system.

Considering the above, a control and modulation approach needs to be able to simultaneously address all the demanding control objectives of the complex higher-order systems in question to the greatest possible extent. A strong candidate for this is model predictive control (MPC) with optimized pulse patterns (OPPs). Such a solution can take advantage of the features of MPC, such as its MIMO nature, its ability to handle explicit constraints, and its high bandwidth that enables fast transients and excellent disturbance rejection [6], [7], and combine them with the excellent steady-state performance of OPPs, as they can produce the theoretical minimum current distortions [8], [9].

In this direction, the method proposed in [10] for MV drives—referred to as model predictive pulse pattern control (MP^{3}C)—employed MPC with OPPs to produce stator currents with very low harmonic distortions, while achieving very fast transients. The experimental assessment of MP^{3}C based on an industrial MV drive clearly demonstrated its superior performance compared with established industrial solutions [11]. Extension of this method, however, to address multiple control objectives and more complex systems is challenging, while it can be conceptually very complicated [12]–[14]. On the other hand, the MPC-based method with OPPs proposed in [15]—referred to as gradient-based predictive pulse pattern control (GP^{3}C)—has high versatility. This is due to the fact that the system dynamics are described by the gradient of the output vector, and the optimization problem underlying GP^{3}C aims at the minimization of the (approximate)

[1]In practice, when MV applications are concerned, the power converter is connected to the grid via an LC filter and a (step-down) transformer. As the transformer has inductive behavior, a filter in LCL configuration can be considered between the converter and the grid.

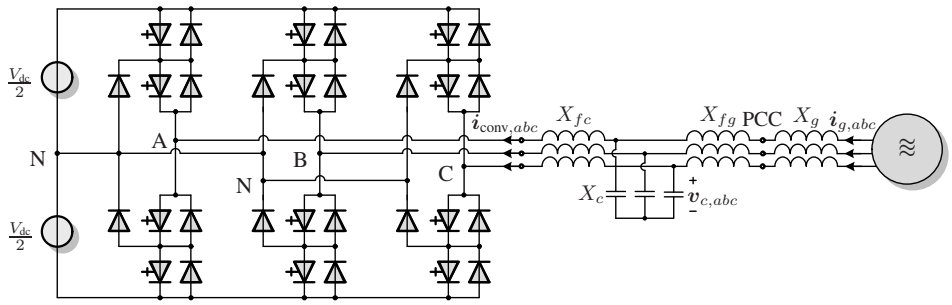

Fig. 1: Three-level NPC converter connected to the grid via an LCL filter.

rms output error. As a result, generalization of the method to higher-order systems with MIMO characteristics is greatly facilitated.

Motivated by the above, this work develops a control and modulation method in the framework of GP^{3}C for MV grid-connected converters with LCL filters. To this aim, GP^{3}C is refined to tackle the MIMO nature of the system. More specifically, the output gradient that acts as the prediction model is computed to account for the evolution of all controlled variables, namely the grid and converter currents, and filter capacitor voltage. Moreover, a sufficiently long prediction horizon, combined with the full state information, provides active damping, rendering additional damping loops unnecessary. As a result, the MV system can be operated at a very low device switching frequency, and below the filter resonance frequency, while still producing high-quality currents that meet the relevant harmonic grid codes. The presented comparison with conventional linear control with SVM demonstrates the benefits of the proposed control algorithm.

II. Model of the Grid-Connected Converter with an LCL Filter

Consider the MV system consisting of a three-level neutral-point-clamped (NPC) converter connected to the grid via an LCL filter as shown in Fig. 1. To keep the controller analysis simple, the dc-link voltage $V_{\rm dc}$ is assumed to be constant, and the neutral point potential fixed to zero. With these assumptions, the output converter voltage in phase x, with $x \in \{a, b, c\}$, can assume the values $-V_{\rm dc}/2$, 0, or $V_{\rm dc}/2$, depending on the *single-phase* switch position $u_x \in \{-1, 0, 1\}$.

As the proposed control problem is designed in the stationary orthogonal $\alpha\beta$ system, any variable in the abc-plane $\boldsymbol{\xi}_{abc} = [\xi_a \ \xi_b \ \xi_c]^T$ needs to be mapped into a two-dimensional vector $\boldsymbol{\xi}_{\alpha\beta} = [\xi_\alpha \ \xi_\beta]^T$ in the $\alpha\beta$-plane via the transformation matrix $\boldsymbol{K}$, i.e., $\boldsymbol{\xi}_{\alpha\beta} = \boldsymbol{K}\boldsymbol{\xi}_{abc}$, with

$$\boldsymbol{K} = \frac{2}{3}\begin{bmatrix} 1 & -\frac{1}{2} & -\frac{1}{2} \\ 0 & \frac{\sqrt{3}}{2} & -\frac{\sqrt{3}}{2} \end{bmatrix}.$$

Therefore, the converter voltage in the $\alpha\beta$-plane is given by[2]

$$\boldsymbol{v}_{\rm conv}(t) = \frac{V_{\rm dc}}{2}\boldsymbol{K}\boldsymbol{u}_{abc}(t)\,, \tag{1}$$

[2]Throughout the paper, vectors in the abc-plane are denoted with the corresponding subscript. On the other hand, the subscript for vectors in the $\alpha\beta$-plane is omitted.

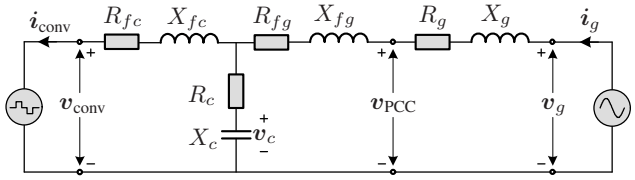

Fig. 2: Equivalent circuit of a three-level converter connected to the grid via an LCL filter in the stationary ($\alpha\beta$) plane.

where $\boldsymbol{u}_{abc} = [u_a \ u_b \ u_c]^T$ is the *three-phase* switch position.

Considering the equivalent circuit representation of the system in question in the $\alpha\beta$-plane (see Fig. 2), the differential equations that describe the dynamics of the system are

$$\frac{\mathrm{d}\boldsymbol{i}_{\rm conv}}{\mathrm{d}t} = \frac{1}{X_{fc}}\big(\boldsymbol{v}_c - (R_{fc}+R_c)\boldsymbol{i}_{\rm conv} + R_c\boldsymbol{i}_g - \boldsymbol{v}_{\rm conv}\big)\,, \tag{2a}$$

$$\frac{\mathrm{d}\boldsymbol{i}_g}{\mathrm{d}t} = \frac{1}{X_{gr}}\big(\boldsymbol{v}_g - (R_{gr}+R_c)\boldsymbol{i}_g + R_c\boldsymbol{i}_{\rm conv} - \boldsymbol{v}_c\big)\,, \tag{2b}$$

$$\frac{\mathrm{d}\boldsymbol{v}_c}{\mathrm{d}t} = \frac{1}{X_c}(\boldsymbol{i}_g - \boldsymbol{i}_{\rm conv})\,, \tag{2c}$$

$$\frac{\mathrm{d}\boldsymbol{v}_g}{\mathrm{d}t} = \omega_g\begin{bmatrix} 0 & -1 \\ 1 & 0 \end{bmatrix}\boldsymbol{v}_g\,, \tag{2d}$$

where the variables of interest are the converter current $\boldsymbol{i}_{\rm conv}$, grid current $\boldsymbol{i}_g$, capacitor voltage $\boldsymbol{v}_c$, and grid voltage $\boldsymbol{v}_g$. The parameters in (2) are the converter-side filter reactance X_{fc} and resistance R_{fc}, the grid-side equivalent reactance and resistance, $X_{gr} = X_{fg} + X_g$ and $R_{gr} = R_{fg} + R_g$, respectively—where X_{fg} (R_{fg}) and X_g (R_g) are the grid-side filter and grid reactance (resistance), respectively—as well as the reactance X_c and internal resistance R_c of the filter capacitor. Finally, ω_g is the angular grid frequency. Note that the system is modeled in per unit (p.u.), thus all SI variables are normalized based on the rated values of the system.

Let the three-phase switch position be the system input, the converter current, grid current, filter capacitor voltage, and grid voltage comprise the system state, i.e., $\boldsymbol{x} = [\boldsymbol{i}_{\rm conv}^T \ \boldsymbol{i}_g^T \ \boldsymbol{v}_c^T \ \boldsymbol{v}_g^T]^T \in \mathbb{R}^8$, and the converter current, grid current, and filter capacitor voltage be the system output, i.e., $\boldsymbol{y} = [\boldsymbol{i}_{\rm conv}^T \ \boldsymbol{i}_g^T \ \boldsymbol{v}_c^T]^T \in \mathbb{R}^6$. With the help of (2), the continuous-time state-space model of the system is of the form

$$\frac{\mathrm{d}\boldsymbol{x}(t)}{\mathrm{d}t} = \boldsymbol{F}\boldsymbol{x}(t) + \boldsymbol{G}\boldsymbol{u}_{abc}(t) \tag{3a}$$

$$\boldsymbol{y}(t) = \boldsymbol{C}\boldsymbol{x}(t)\,, \tag{3b}$$

where the system $\boldsymbol{F} \in \mathbb{R}^{8\times8}$, input $\boldsymbol{G} \in \mathbb{R}^{8\times3}$, and output $\boldsymbol{C} \in \mathbb{R}^{6\times8}$ matrices are provided in Appendix A.

Finally, as MPC is developed in the discrete-time domain, (3) is discretized with the sampling interval T_s. This yields

$$\boldsymbol{x}(k+1) = \boldsymbol{A}\boldsymbol{x}(k) + \boldsymbol{B}\boldsymbol{u}_{abc}(k) \tag{4a}$$

$$\boldsymbol{y}(k) = \boldsymbol{C}\boldsymbol{x}(k)\,, \tag{4b}$$

where $k \in \mathbb{N}^+$ denotes the discrete time step. Note that the matrices $\boldsymbol{A}$ and $\boldsymbol{B}$ in (4) are derived by using forward Euler discretization.

III. GP^{3}C as a MIMO Controller

The discussed control algorithm, i.e., GP^{3}C, is based on two pillars, namely OPPs [8], [9], and gradient-based MPC [16], [17]. The former ensures the best possible steady-state performance in terms of grid current distortions, while the high versatility of the latter enables the design of a simple yet effective MIMO control approach. These aspects are presented in more detail in the sequel of this section.

A. OPPs for Higher-Order Systems

OPPs are computed in an offline procedure by solving an optimization problem that aims to minimize the current distortions of the load current. In doing so, the lowest possible harmonic current results for a given pulse number d, i.e., ratio of switching-to-fundamental frequency. This problem is solved for several modulation indices to cover the whole range of operating points. Moreover, quarter- and half-wave symmetry is imposed on the pulse patterns, while three-phase symmetry is assumed. This means that for a given modulation index $m \in [0, \pi/4]$, and considering a specific sequence of switch positions, it suffices to compute the instants—referred to as switching angles—where a switching event occurs within the first quarter of the fundamental period. Hence, the result of the optimization procedure is a set of d switching angles in the range $[0, 90^o]$ that fully define the OPP $\boldsymbol{p}(d, m)$.

Nevertheless, OPPs are typically computed by assuming an inductive load. As a result, when used with higher-order systems, such as the system in question (see Fig. 1), their benefits can be compromised. For this reason, the OPPs in this work are computed to account for the LCL filter by considering the transfer function from the switching function harmonics to the grid current harmonics [18], see Fig. 3. In doing so, the OPPs produce grid currents that not only have the lowest possible TDD, but also meet harmonic grid standards, such as the IEEE 519 [19], even at very low pulse numbers.

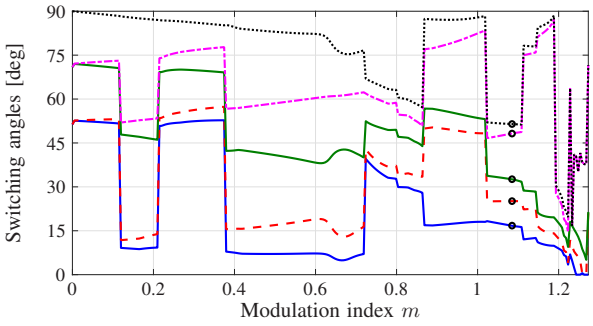

(a) Optimal switching angles for $d = 5$. The (black) circles indicate the switching angles for $m = 1.085$.

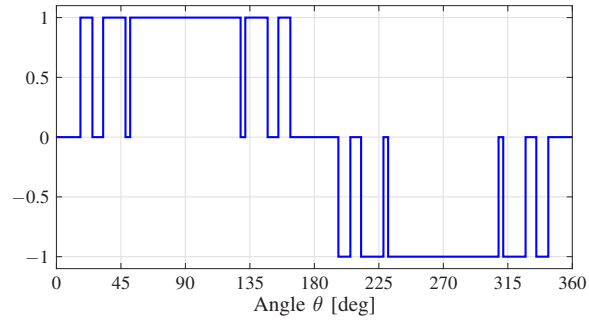

(b) Single-phase OPP $u(\theta)$ at $m = 1.085$ and $d = 5$, i.e., $\boldsymbol{p}(5, 1.085)$.

Fig. 3: Optimization results of a three-level OPP problem that considers the transfer function from the switching function harmonics to the grid current harmonics. The pulse number is $d = 5$ and quarter and half-wave symmetry is imposed on the OPP.

B. Control Problem

The proposed MIMO control strategy is designed in the $\alpha\beta$-plane. It aims at regulating the output vector $\boldsymbol{y}$ along its reference trajectory $\boldsymbol{y}_{\text{ref}}$. To do so, the switching instants of the nominal OPP are manipulated in real time such that favorable performance is achieved. More specifically, the controller manipulates the $z \in \mathbb{N}^+$ switching time instants of the nominal OPP that fall within a time window T_p such that the rms error of *all* output variables is minimized. This time window can be interpreted as the prediction horizon, and it is an integer multiple of the sampling interval T_s, i.e., $T_p = N_p T_s$, where N_p denotes the number of prediction horizon steps.

To devise the controller based on the above description, let

$$\boldsymbol{t} = \begin{bmatrix} t_1 & t_2 & \dots & t_z \end{bmatrix}^T \in \mathbb{R}^z$$

be the vector of the (to-be-computed) modified switching time instants that fall within T_p, and

$$\boldsymbol{t}_{\text{ref}} = \begin{bmatrix} t_{1,\text{ref}} & t_{2,\text{ref}} & \dots & t_{z,\text{ref}} \end{bmatrix}^T \in \mathbb{R}^z$$

the vector of the corresponding nominal OPP switching time instants. The aforementioned control objectives can be mathematically described with an objective function of the form

$$J = \sum_{i=1}^{z} \|\boldsymbol{y}_{\text{ref}}(t_{i,\text{ref}}) - \boldsymbol{y}(t_i)\|^2_{\boldsymbol{Q}} + \lambda_t \|\Delta \boldsymbol{t}\|_2^2\,, \tag{5}$$

where the first term relates to the output trajectory tracking problem as it accounts for the weighted (squared) rms error of the system output. Note that, as shown in [16], this term is a simplification of a continuous-time integration of the output error over T_p. According to Parseval's theorem, such an integral captures the harmonic energy of the output error. Hence, minimizing (5) is equivalent to minimizing the TDD of the output variables. Moreover, as can be seen, the output

error is weighted by the diagonal entries of the positive definite matrix $\boldsymbol{Q} = \mathrm{diag}(\boldsymbol{I}_2 q_{i_{\mathrm{conv}}}, \boldsymbol{I}_2 q_{i_g}, \boldsymbol{I}_2 q_{v_c}) \in \mathbb{R}^{6\times 6}$. Thus, these entries penalize the deviation of the output variables from their respective reference trajectories, where the weighting factors $q_{i_{\mathrm{conv}}}, q_{v_c}, q_{i_g} > 0$ set the priority among the tracking of the trajectories of the different output variables, and $\boldsymbol{I}_2$ is the two-dimensional identity matrix. As for the second term in (5), it models the deviation of the to-be-computed switching time instants from their nominal values, i.e., $\Delta \boldsymbol{t} = \boldsymbol{t}_{\mathrm{ref}} - \boldsymbol{t}$. Therefore, this term enables the manipulation of the changes in the nominal switching time instants of the (offline-computed) OPP by means of the weighting factor $\lambda_t > 0$.

According to (5), the evolution of the output $\boldsymbol{y}$ needs to be computed within the subintervals of the prediction horizon $[0, t_{1,\mathrm{ref}})$, $[t_{1,\mathrm{ref}}, t_{2,\mathrm{ref}})$, $[t_{2,\mathrm{ref}}, t_{3,\mathrm{ref}})$, $\ldots$, and $[t_{z,\mathrm{ref}}, T_p)$. This can be done with the help of (4) and the (known) sequence of OPP switch positions within T_p

$$\boldsymbol{U} = \begin{bmatrix} \boldsymbol{u}_{abc}^T(t_0) & \boldsymbol{u}_{abc}^T(t_{1,\mathrm{ref}}) & \ldots & \boldsymbol{u}_{abc}^T(t_{z,\mathrm{ref}}) \end{bmatrix}^T . \tag{6}$$

By considering, however, that the interval between two consecutive OPP switching time instants is relatively small, i.e.,

$$t_{i+1,\mathrm{ref}} - t_{i,\mathrm{ref}} \ll T_1, \forall i \in \{1, \ldots, 4d-1\} ,$$

where T_1 is the fundamental period, the prediction task can be significantly simplified. Specifically, the output trajectory within the subintervals of the prediction horizon can be provided by the corresponding gradients, i.e.,

$$\begin{aligned} \boldsymbol{m}(t_{\ell,\mathrm{ref}}) = \frac{\mathrm{d}\boldsymbol{y}(t_{\ell,\mathrm{ref}})}{\mathrm{d}t} &\approx \frac{\boldsymbol{y}(t_{\ell+1,\mathrm{ref}}) - \boldsymbol{y}(t_{\ell,\mathrm{ref}})}{\Delta t_{\ell,\mathrm{ref}}} \\ &= \boldsymbol{C} \frac{\boldsymbol{x}(t_{\ell+1,\mathrm{ref}}) - \boldsymbol{x}(t_{\ell,\mathrm{ref}})}{\Delta t_{\ell,\mathrm{ref}}} , \end{aligned} \tag{7}$$

where

$$\Delta t_{\ell,\mathrm{ref}} = t_{\ell+1,\mathrm{ref}} - t_{\ell,\mathrm{ref}} ,$$

$\ell \in \{0, 1, \ldots, z-1\}$, and $t_{0,\mathrm{ref}} \equiv t_0 \equiv kT_s$. Note that in (7), the discrete-time state-space model (4) is revised to

$$\boldsymbol{x}(t_{\ell+1,\mathrm{ref}}) = \boldsymbol{A}\boldsymbol{x}(t_{\ell,\mathrm{ref}}) + \boldsymbol{B}\boldsymbol{u}_{abc}(t_{\ell,\mathrm{ref}}) \tag{8a}$$

$$\boldsymbol{y}(t_{\ell,\mathrm{ref}}) = \boldsymbol{C}\boldsymbol{x}(t_{\ell,\mathrm{ref}}) , \tag{8b}$$

and the system matrices are discretized with $\Delta t_{\ell,\mathrm{ref}}$. Thus, expression (7) equips the controller with great design versatility, as the gradient vectors can be easily computed regardless of whether the system is linear or nonlinear [20], simple (e.g., first-order system), or complex (e.g., higher-order system). The evolution of the trajectory of one arbitrary output variable is visualized in Fig. 4.

With the prediction model (7), and after some algebraic manipulations that are provided in Appendix B, function (5) can be written as

$$J = \|\boldsymbol{r} - \boldsymbol{M}\boldsymbol{t}\|_{\widetilde{\boldsymbol{Q}}}^2 + \lambda_t \|\Delta \boldsymbol{t}\|_2^2 , \tag{9}$$

where $\boldsymbol{r}$ is a vector that depends on the reference values and measurements of the output, and $\boldsymbol{M}$ is a matrix whose nonzero entries depend on the gradients with which the controlled (i.e., output) variables evolve over the prediction horizon T_p. The detailed form of $\boldsymbol{r}$ and $\boldsymbol{M}$ is presented in Appendix B. It is noteworthy that the dimensions of $\boldsymbol{r}$ and $\boldsymbol{M}$ change with time as they depend on the number of the OPP switching time instants that fall within the horizon, i.e., $\boldsymbol{r} \in \mathbb{R}^{6z}$ and $\boldsymbol{M} \in \mathbb{R}^{6z\times z}$. Finally, matrix $\widetilde{\boldsymbol{Q}}$ is block diagonal and it is given by $\widetilde{\boldsymbol{Q}} = \mathrm{diag}(\boldsymbol{Q}, \ldots, \boldsymbol{Q}) \in \mathbb{R}^{6z\times 6z}$.

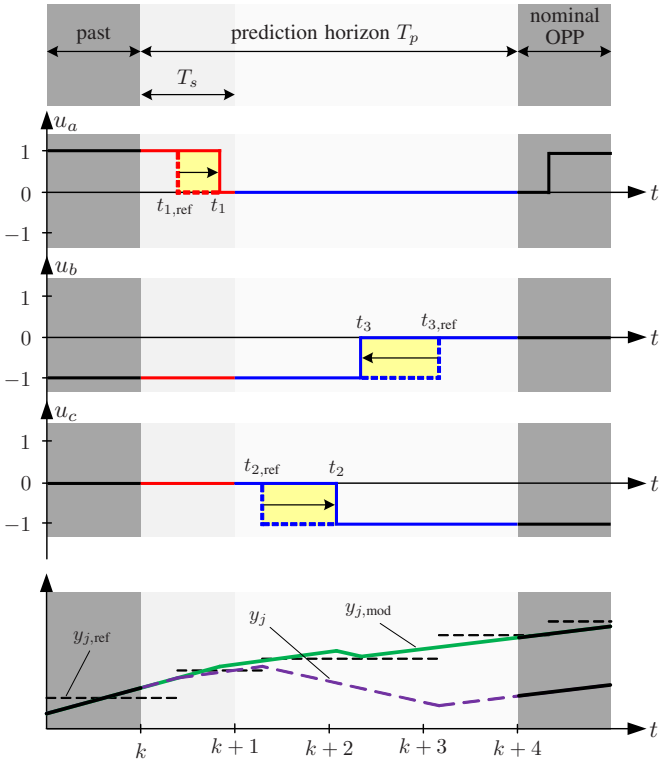

Fig. 4: Example of the evolution of one (arbitrary) controlled variable (e.g., the α-component of the grid current) within a four-step ($T_p = 4T_s$) prediction horizon when applying the depicted pulse pattern. Top part: The modifications on the offline-computed, nominal OPP, as introduced by the controller, are shown with arrows, while the modified volt-second area is also highlighted. Bottom part: The (linearized) trajectory of the controlled variable when applying the nominal OPP is shown with the dash-dotted (magenta) line, while its (linearized) trajectory when applying the modified pulse pattern is shown with the solid (green) line. The dashed (black) line shows the reference sampled at the nominal OPP time instants.

C. Control Algorithm

The block diagram of the proposed control algorithm is presented in Fig. 5. In the sequel of this section the depicted individual blocks discussed.

1) Outer Control Loop: In a first step, the desired values of the controlled variables are derived. A dc-link voltage controller is employed to control the dc-link voltage V_{dc} by manipulating the active power reference P_{ref}. The reactive power reference value Q_{ref} is set by considering the desired power factor, which is typically set equal to one. With P_{ref} and Q_{ref}, and a given grid angular frequency ω_g, the operating point is defined. Following, as per [6, Chapter 6.3], the (time-varying) output reference values can be computed at steady-state operating conditions by performing a vector analysis in a rotating (dq) reference plane that is aligned with the grid

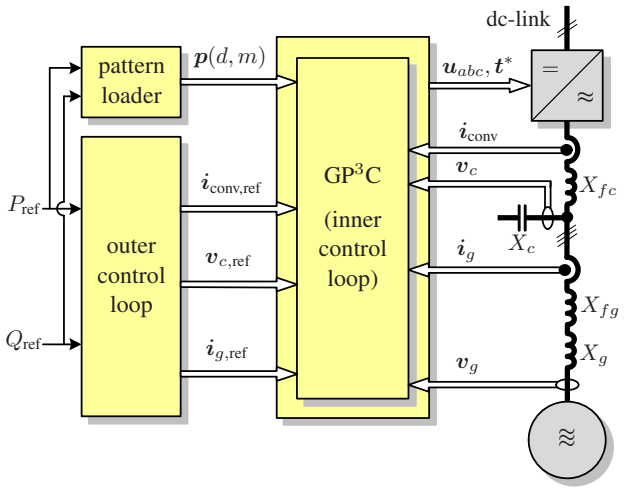

Fig. 5: Block diagram of the GP^{3}C scheme.

Algorithm 1 GP^{3}C for higher-order systems

Given $\boldsymbol{u}_{abc}(t_0^-)$, $\boldsymbol{y}_{\text{ref}}(t_0)$, $\boldsymbol{x}(t_0)$, and $\boldsymbol{p}(d,m)$

0. Extract the switching time instants and switch positions from $\boldsymbol{p}(d,m)$ to formulate $\boldsymbol{t}_{\text{ref}}$ and $\boldsymbol{U}$.
1. Generate the output reference trajectory $\boldsymbol{Y}_{\text{ref}}$ within the horizon T_p to formulate the vector $\boldsymbol{r}$.
2. Formulate the matrix $\boldsymbol{M}$ by computing the gradient vectors $\boldsymbol{m}(t_{\ell,\text{ref}})$, $\ell \in \{0,1,\ldots,z-1\}$.
3. Solve the constrained QP (12). This yields $\boldsymbol{t}^*$.

Return $\boldsymbol{t}^*(k)$ that fall within T_p and modify the OPP accordingly.

voltage $\boldsymbol{v}_g$ (or grid virtual flux $\boldsymbol{\psi}_g$). For a more detailed derivation of the reference values, the reader is referred to [21].

2) Pattern Loader: From the aforementioned steady-state analysis, the converter voltage $\boldsymbol{v}_{\text{conv}}$ required to achieve the desired reference tracking is also derived. Hence, the modulation index m is chosen as

$$m = \frac{2}{V_{\text{dc}}} \|\boldsymbol{v}_{\text{conv}}\|_2 \,. \tag{10}$$

As for the pulse number d, this is decided by considering that the device switching frequency f_{sw} of MV converters should be low, typically below a maximum value $f_{\text{sw,max}}$. At the same time, however, f_{sw} needs to be as high as possible such that the produced current distortions are kept low. Given that for a three-level inverter the device switching frequency is given by $f_{\text{sw}} = d\, f_1$, where f_1 is the fundamental frequency, the pulse number d is selected as the largest integer that is less than the ratio $f_{\text{sw,max}}/f_1$, i.e.,

$$d = \left\lfloor \frac{f_{\text{sw,max}}}{f_1} \right\rfloor = \text{floor}\left(\frac{f_{\text{sw,max}}}{f_1} \right), \tag{11}$$

see also [6, Chapter 12.4].

Following, the pair $\{m, d\}$ is fed into a look-up-table (LUT) to retrieve the desired nominal OPP $\boldsymbol{p}(d,m)$. This OPP is subsequently sent to the inner, GP^{3}C-based controller.

TABLE I: Rated values of the system

Parameter	Symbol	SI Value
Voltage	V_R	3.15 kV
Current	I_R	1.65 kA
Power	P_R	9 MVA
Angular grid frequency	ω_{gR}	$2\pi 50$ rad/s

TABLE II: System parameters

Grid	Reactance	X_g	0.0995
	Resistance	R_g	0.0071
LCL filter	Grid-side reactance	X_{fg}	0.1500
	Grid-side resistance	R_{fg}	0.0150
	Converter-side reactance	X_{fc}	0.0997
	Converter-side resistance	R_{fc}	0.0003
	Capacitance reactance	X_c	0.1455
	Capacitance resistance	R_c	0.0036
Converter	Dc-link	V_{dc}	1.8818

3) GP^{3}C: With the info about the OPP $\boldsymbol{p}(d,m)$, the switching time instants that fall within T_p are retrieved along with the corresponding nominal OPP switch positions. In a next step, the output gradient matrix $\boldsymbol{M}$ is computed based on the retrieved nominal OPP switch positions $\boldsymbol{U}$ (see (6)) and the system dynamics (8). Similarly, the reference vector $\boldsymbol{r}$ is derived based on the output reference vector $\boldsymbol{y}_{\text{ref}}$ within the horizon. Note that the values of $\boldsymbol{y}_{\text{ref}}$ used in the prediction horizon result by sampling the corresponding (sinusoidal) waveforms of the reference quantities at the nominal OPP time instants, giving rise to the reference vector

$$\boldsymbol{Y}_{\text{ref}}(k) = \begin{bmatrix} \boldsymbol{y}_{\text{ref}}^T(t_{1,\text{ref}}) & \boldsymbol{y}_{\text{ref}}^T(t_{2,\text{ref}}) & \ldots & \boldsymbol{y}_{\text{ref}}^T(t_{z,\text{ref}}) \end{bmatrix}^T,$$

see also Appendix B.

Subsequently, the following optimization problem underlying GP^{3}C is formulated based on (9)

$$\begin{aligned} \underset{\boldsymbol{t} \in \mathbb{R}^z}{\text{minimize}} \quad & \|\boldsymbol{r} - \boldsymbol{M}\boldsymbol{t}\|_{\widetilde{\boldsymbol{Q}}}^2 \\ \text{subject to} \quad & kT_s < t_1 < t_2 < \ldots < kT_s + T_p \,. \end{aligned} \tag{12}$$

This problem is solved to find the *optimal* modified switching instants $\boldsymbol{t}^* = [t_1^* \; t_2^* \; \ldots \; t_z^*]^T$.

Finally, in line with the receding horizon policy, only these OPP switch positions $\boldsymbol{u}_{abc}$ that fall within the first sampling interval T_s of T_p are applied to the converter at the corresponding time instants $\boldsymbol{t}^*$, while the switch positions and time instant modifications within the interval $T_p - T_s$ are discarded. In the next iteration, the whole procedure is repeated from the beginning based on new measurements.

The structure of the proposed GP^{3}C scheme is summarized in Algorithm 1. It is worth mentioning that even though GP^{3}C is formulated as a MIMO controller in this work, its core routines remain the same. Moreover, and more importantly, as can be deduced from (12), regardless of the increased number of controlled variables, GP^{3}C is still formulated as a constrained quadratic program (QP). This enables the use of tailored solvers that exploit the geometry of the said

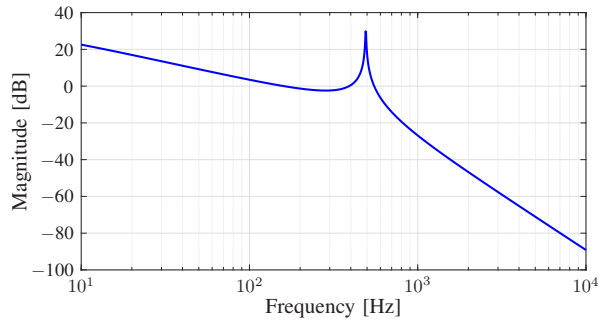

(a) Bode magnitude plot

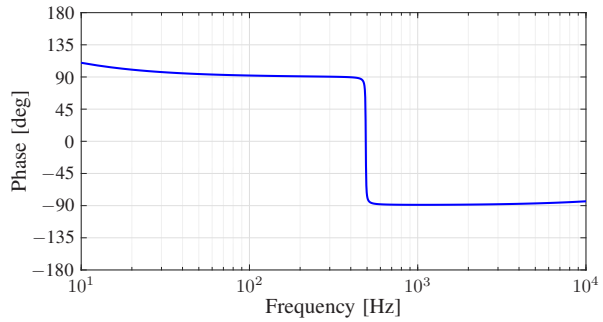

(b) Bode phase plot

Fig. 6: Frequency response of the LCL filter.

QP, see [22]. Consequently, as shown in [23], the real-time implementation of the control scheme is rendered possible.

IV. Performance Evaluation

The simulation results presented in this section are obtained for the MV system shown in Fig. 1. The rated values and parameters of the system in question are provided in Tables I and II, respectively. As can be deduced from the filter parameters in Table II, the resonance frequency is at $f_{\text{res}} = 491$ Hz, see also Fig. 6. As for the controller parameters, the sampling interval is $T_s = 50\,\mu$s and $N_p = 10$, implying a prediction horizon of $T_p = 500\,\mu$s. The weighting factors are $\boldsymbol{Q} = \text{diag}(1, 1, 5, 5, 20, 20)$ to prioritize the grid current reference tracking, and $\lambda_t = 5 \cdot 10^6$. A three-level OPP with a pulse number $d = 5$ is used such that the device switching frequency is $f_{\text{sw}} = 250$ Hz, i.e., well below f_{res},[3] and the modulation index is $m = 1.085$, see Fig. 3(b). Finally, all results are shown in the p.u. system.

In the following, the steady-state performance of the proposed MIMO control approach at nominal operating conditions ($P_{\text{ref}} = 1$ and $Q_{\text{ref}} = 0$) is illustrated and discussed. The relevant results are shown in Fig. 7. As can be seen in Fig. 7(a), the active and reactive power references are successfully tracked. This is achieved due to the effective operation of the inner, MPC-based loop, as the proposed GP^{3}C scheme simultaneously regulates all three controlled variables, i.e., the converter current, filter capacitor voltage, and grid current along their references, see Figs. 7(b), 7(c), and 7(d), respectively. With regards to the latter, owing to the minute modifications of the OPP (Fig. 7(f)), the grid current TDD is only 1.77%, i.e., very close to its ideal value of 1.57%, and the current harmonics are located at odd, non-triplen integer multiples of f_1, see Fig. 7(e). As a result, harmonic grid standards, such as the IEEE 519, are fully met.

On the other hand, when comparing the harmonic spectrum of the grid current produced by conventional linear control with SVM, it is evident that the performance is not that favorable, see Fig. 8. Specifically, as can be seen in that figure, the amplitude of the low-frequency harmonics is very high, giving rise to a current TDD of 6.55%, i.e., almost four times greater than that of GP^{3}C.

Finally, it should be pointed out that the superior steady-state performance of GP^{3}C is achieved without the presence of an additional active damping loop as this is inherent to the proposed control algorithm. Consequently, the converter apparent switching frequency is almost equal to the filter resonance frequency, implying full utilization of the available hardware, and thus reduced cost of the system.

V. Conclusion

This paper refined the GP^{3}C algorithm introduced in [15] to address the MIMO characteristics of a system consisting of an MV converter connected to the grid via an LCL filter. As shown, the controller exhibits superior performance during steady state, i.e., minimal grid current TDD for a given switching frequency, while operating the system at very low switching frequency (with apparent switching frequency almost equal to the filter resonance frequency) to achieve increased system efficiency and full utilization of the available hardware. This favorable performance is attributed to the effective combination of gradient-based MPC and OPPs. Owing to the former, the adopted versatile prediction model—which relies on the output gradients—enables the full exploitation of the MIMO control nature of MPC. As for the OPPs, they ensure the lowest possible harmonic distortions, especially at very low pulse numbers. Notably, despite the complexity of the control problem in question, the developed control algorithm is characterized by design and conceptual simplicity. These features, along with the fact that the controller is formulated as a QP, facilitate the real-time implementation of the discussed MIMO control strategy.

Appendix A
State-Space Model Matrices

The matrices of the continuous-time state-space model in (3) are

$$\boldsymbol{F} = \begin{bmatrix} -\frac{R_{fc}+R_c}{X_{fc}}\boldsymbol{I}_2 & \frac{R_c}{X_{fc}}\boldsymbol{I}_2 & \frac{1}{X_{fc}}\boldsymbol{I}_2 & \boldsymbol{0}_{2\times 2} \\ \frac{R_c}{X_{gr}}\boldsymbol{I}_2 & -\frac{R_{gr}+R_c}{X_{gr}}\boldsymbol{I}_2 & -\frac{1}{X_{gr}}\boldsymbol{I}_2 & \frac{1}{X_{gr}}\boldsymbol{I}_2 \\ -\frac{1}{X_c}\boldsymbol{I}_2 & \frac{1}{X_c}\boldsymbol{I}_2 & \boldsymbol{0}_{2\times 2} & \boldsymbol{0}_{2\times 2} \\ \boldsymbol{0}_{2\times 2} & \boldsymbol{0}_{2\times 2} & \boldsymbol{0}_{2\times 2} & \omega_g \begin{bmatrix} 0 & -1 \\ 1 & 0 \end{bmatrix} \end{bmatrix}$$

$$\boldsymbol{G} = -\frac{V_{\text{dc}}}{2X_{fc}} \begin{bmatrix} \boldsymbol{I}_2 & \boldsymbol{0}_{2\times 6} \end{bmatrix}^T \boldsymbol{K}, \text{ and } \boldsymbol{C} = \begin{bmatrix} \boldsymbol{I}_6 & \boldsymbol{0}_{6\times 2} \end{bmatrix},$$

[3] This implies that the *apparent* switching frequency of the converter is almost the same as the filter resonance frequency.

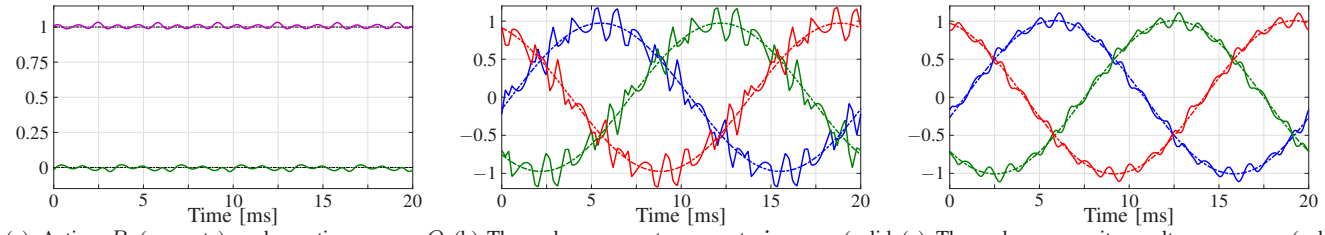

(a) Active P (magenta) and reactive power Q (green) and their references (dash-dotted line).

(b) Three-phase converter currents $\boldsymbol{i}_{\text{conv},abc}$ (solid lines) and their references (dash-dotted lines).

(c) Three-phase capacitor voltages $\boldsymbol{v}_{c,abc}$ (solid lines) and their references (dash-dotted lines).

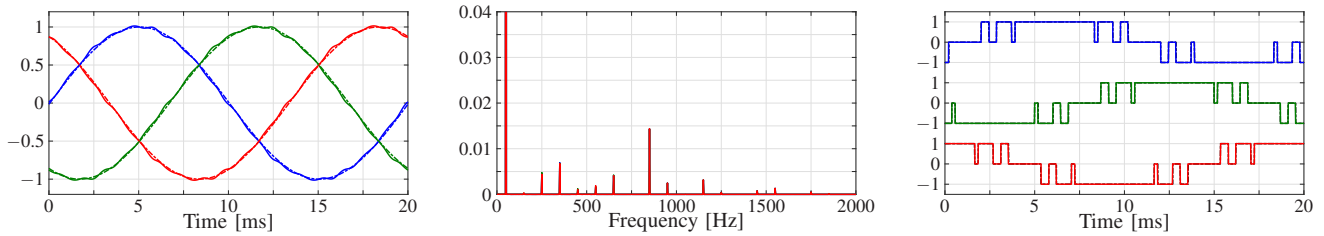

(d) Three-phase grid currents $\boldsymbol{i}_{g,abc}$ (solid lines) and their references (dash-dotted lines).

(e) Grid current spectrum. The TDD is 1.77%.

(f) Three-phase (modified) switching pattern $\boldsymbol{u}_{abc}$ (solid lines) and nominal OPP (dash-dotted lines).

Fig. 7: Simulation results of the proposed GP^{3}C during steady-state operation and unity power factor ($f_{\text{sw}} = 250\,\text{Hz}$).

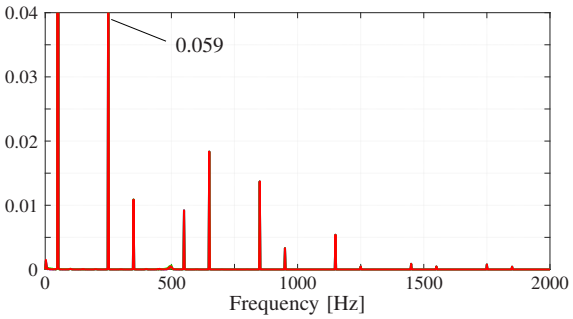

Fig. 8: Grid current harmonic spectrum produced by linear control and SVM. The TDD is 6.55%.

where $\boldsymbol{I}$ and $\boldsymbol{0}$ are the identity and zero matrices, respectively, the dimensions of which are denoted by the corresponding subscripts.

Appendix B
Derivation of the Objective Function in Vector Form

The first term of the objective function (5) can be written as

$$J_1 = \|\boldsymbol{y}_{\text{ref}}(t_{1,\text{ref}}) - \boldsymbol{y}(t_1)\|^2_{\boldsymbol{Q}} + \|\boldsymbol{y}_{\text{ref}}(t_{2,\text{ref}}) - \boldsymbol{y}(t_2)\|^2_{\boldsymbol{Q}} + \ldots + \|\boldsymbol{y}_{\text{ref}}(t_{z,\text{ref}}) - \boldsymbol{y}(t_z)\|^2_{\boldsymbol{Q}}\,, \tag{13}$$

where $\boldsymbol{y}_{\text{ref}}(t_{\ell,\text{ref}})$, $\ell \in \{1, 2, \ldots, z\}$, is the vector of reference values sampled as the nominal OPP time instants $t_{\ell,\text{ref}}$ and

$$\begin{aligned}
\boldsymbol{y}(t_1) &= \boldsymbol{y}(t_0) + \boldsymbol{m}(t_{0,\text{ref}})\, t_1\,,\\
\boldsymbol{y}(t_2) &= \boldsymbol{y}(t_1) + \boldsymbol{m}(t_{1,\text{ref}})\,(t_2 - t_1)\\
&= \boldsymbol{y}(t_0) + \boldsymbol{m}_0\, t_1 + \boldsymbol{m}(t_{1,\text{ref}})\, t_2\,,\\
&\vdots\\
\boldsymbol{y}(t_z) &= \boldsymbol{y}(t_{z-1}) + \boldsymbol{m}(t_{z-1,\text{ref}})\,(t_z - t_{z-1})\\
&= \boldsymbol{y}(t_0) + \boldsymbol{m}_0\, t_1 + \ldots + \boldsymbol{m}_{z-2}\, t_{z-1} + \boldsymbol{m}(t_{z-1,\text{ref}})\, t_z\,,
\end{aligned}$$

with $\boldsymbol{m}_\ell = \boldsymbol{m}(t_{\ell,\text{ref}}) - \boldsymbol{m}(t_{\ell+1,\text{ref}})$ for $\ell \in \{0, 1, \ldots, z-2\}$. Thus, with the above, function (13) can be written in the following vector form, as presented in (9), i.e.,

$$J_1 = \left\| \underbrace{\begin{bmatrix} \boldsymbol{y}_{\text{err}}(t_{1,\text{ref}}) \\ \boldsymbol{y}_{\text{err}}(t_{2,\text{ref}}) \\ \vdots \\ \boldsymbol{y}_{\text{err}}(t_{z,\text{ref}}) \end{bmatrix}}_{\boldsymbol{r}} - \underbrace{\begin{bmatrix} \boldsymbol{m}_{t_0} & \boldsymbol{0}_6 & \cdots & \boldsymbol{0}_6 & \boldsymbol{0}_6 \\ \boldsymbol{m}_0 & \boldsymbol{m}_{t_1} & \cdots & \boldsymbol{0}_6 & \boldsymbol{0}_6 \\ \vdots & \vdots & \ddots & \vdots & \vdots \\ \boldsymbol{m}_0 & \boldsymbol{m}_1 & \cdots & \boldsymbol{m}_{t_{z-2}} & \boldsymbol{0}_6 \\ \boldsymbol{m}_0 & \boldsymbol{m}_1 & \cdots & \boldsymbol{m}_{z-2} & \boldsymbol{m}_{t_{z-1}} \end{bmatrix}}_{\boldsymbol{M}} \underbrace{\begin{bmatrix} t_1 \\ t_2 \\ \vdots \\ t_z \end{bmatrix}}_{\boldsymbol{t}} \right\|^2_{\tilde{\boldsymbol{Q}}},$$

where $\boldsymbol{y}_{\text{err}}(t_{\ell,\text{ref}}) = \boldsymbol{y}_{\text{ref}}(t_{\ell,\text{ref}}) - \boldsymbol{y}(t_0)$, $\ell \in \{1, 2, \ldots, z\}$, and $\boldsymbol{m}_{t_\ell} = \boldsymbol{m}(t_{\ell,\text{ref}})$, $\ell \in \{1, 2, \ldots, z-1\}$.

Acknowledgment

This work was supported by the Academy of Finland.

References

[1] M. Liserre, F. Blaabjerg, and S. Hansen, "Design and control of an LCL-filter-based three-phase active rectifier," *IEEE Trans. Ind. Appl.*, vol. 41, no. 5, pp. 1281–1291, Sep./Oct. 2005.

[2] D. G. Holmes and T. A. Lipo, *Pulse width modulation for power converters: Principles and practice*. Piscataway, NJ, USA: IEEE Press, 2003.

[3] J. Holtz, "Pulsewidth modulation for electronic power conversion," *Proc. IEEE*, vol. 82, no. 8, pp. 1194–1214, Aug. 1994.

[4] J. Dannehl, F. W. Fuchs, S. Hansen, and P. B. Thøgersen, "Investigation of active damping approaches for PI-based current control of grid-connected pulse width modulation converters with LCL filters," *IEEE Trans. Ind. Appl.*, vol. 46, no. 4, pp. 1509–1517, Jul./Aug. 2010.

[5] S. G. Parker, B. P. McGrath, and D. G. Holmes, "Regions of active damping control for LCL filters," *IEEE Trans. Ind. Appl.*, vol. 50, no. 1, pp. 424–432, Jan./Feb. 2014.

[6] T. Geyer, *Model predictive control of high power converters and industrial drives*. Hoboken, NJ, USA: Wiley, 2016.

[7] P. Karamanakos, E. Liegmann, T. Geyer, and R. Kennel, "Model predictive control of power electronic systems: Methods, results, and challenges," *IEEE Open J. Ind. Appl.*, vol. 1, pp. 95–114, 2020.

[8] G. S. Buja and G. B. Indri, "Optimal pulsewidth modulation for feeding ac motors," *IEEE Trans. Ind. Appl.*, vol. IA-13, no. 1, pp. 38–44, Jan./Feb. 1977.

[9] G. S. Buja, "Optimum output waveforms in PWM inverters," *IEEE Trans. Ind. Appl.*, vol. IA-16, no. 6, pp. 830–836, Nov./Dec. 1980.

[10] T. Geyer, N. Oikonomou, G. Papafotiou, and F. D. Kieferndorf, "Model predictive pulse pattern control," *IEEE Trans. Ind. Appl.*, vol. 48, no. 2, pp. 663–676, Mar./Apr. 2012.

[11] N. Oikonomou, C. Gutscher, P. Karamanakos, F. D. Kieferndorf, and T. Geyer, "Model predictive pulse pattern control for the five-level active neutral-point-clamped inverter," *IEEE Trans. Ind. Appl.*, vol. 49, no. 6, pp. 2583–2592, Nov./Dec. 2013.

[12] M. Vasiladiotis, A. Christe, and T. Geyer, "Model predictive pulse pattern control for modular multilevel converters," *IEEE Trans. Ind. Electron.*, vol. 66, no. 3, pp. 2423–2431, Mar. 2019.

[13] V. Spudić and T. Geyer, "Model predictive control based on optimized pulse patterns for modular multilevel converter STATCOM," *IEEE Trans. Ind. Appl.*, vol. 55, no. 6, pp. 6137–6149, Nov./Dec. 2019.

[14] M. Dorfling, H. Mouton, and T. Geyer, "Generalized model predictive pulse pattern control based on small-signal modeling—Part 1: Algorithm," *IEEE Trans. Power Electron.*, vol. 37, no. 9, pp. 10 476–10 487, Sep. 2022.

[15] M. A. W. Begh, P. Karamanakos, and T. Geyer, "Gradient-based predictive pulse pattern control of medium-voltage drives—Part I: Control, concept, and analysis," *IEEE Trans. Power Electron.*, vol. 37, no. 12, pp. 14 222–14 236, Dec. 2022.

[16] P. Karamanakos, R. Mattila, and T. Geyer, "Fixed switching frequency direct model predictive control based on output current gradients," in *Proc. IEEE Ind. Electron. Conf.*, Washington, D.C., USA, Oct. 2018, pp. 2329–2334.

[17] P. Karamanakos, M. Nahalparvari, and T. Geyer, "Fixed switching frequency direct model predictive control with continuous and discontinuous modulation for grid-tied converters with LCL filters," *IEEE Trans. Control Syst. Technol.*, vol. 29, no. 4, pp. 1503–1518, Jul. 2021.

[18] S. Rahmanpour, P. Karamanakos, and T. Geyer, "Three-level optimized pulse patterns for grid-connected converters with LCL filters," in *Proc. IEEE Energy Convers. Congr. Expo.*, Nashville, TN, USA, Oct./Nov. 2023, pp. 1–8.

[19] IEEE Std 519-2014 (Revision of IEEE Std 519-1992), "IEEE recommended practices and requirements for harmonic control in electrical power systems," pp. 1–29, Jun. 2014.

[20] M. A. W. Begh, P. Karamanakos, and T. Geyer, "Gradient-based predictive pulse pattern control with active neutral point balancing for three-level inverter medium-voltage drives," in *Proc. IEEE Energy Convers. Congr. Expo.*, Detroit, MI, USA, Oct. 2022, pp. 1–8.

[21] M. Rossi, P. Karamanakos, and F. Castelli-Dezza, "An indirect model predictive control method for grid-connected three-level neutral point clamped converters with LCL filters," *IEEE Trans. Ind. Appl.*, vol. 58, no. 3, pp. 3750–3768, May/Jun. 2022.

[22] Q. Yang, P. Karamanakos, W. Tian, X. Gao, X. Li, T. Geyer, and R. Kennel, "Computationally efficient fixed switching frequency direct model predictive control," *IEEE Trans. Power Electron.*, vol. 37, no. 3, pp. 2761–2777, Mar. 2022.

[23] M. A. W. Begh, P. Karamanakos, T. Geyer, and Q. Yang, "Gradient-based predictive pulse pattern control of medium-voltage drives—Part II: Performance assessment," *IEEE Trans. Power Electron.*, vol. 37, no. 12, pp. 14 237–14 251, Dec. 2022.